GEOPHYSICAL RESEARCH LETTERS, VOL. 39, L18105, doi:10.1029/2012GL053168, 2012

A high-resolution model of field-aligned currents through empirical orthogonal functions analysis (MFACE)

Maosheng He,[1] Joachim Vogt,[1] Hermann Lühr,[2] Eugen Sorbalo,[1] Adrian Blagau,[1,3] Guan Le,[4] and Gang Lu[5]

Received 17 July 2012; revised 14 August 2012; accepted 14 August 2012; published 26 September 2012.

[1] Ten years of CHAMP magnetic field measurements are integrated into MFACE, a model of field-aligned currents (FACs) using empirical orthogonal functions (EOFs). EOF1 gives the basic Region-1/Region-2 pattern varying mainly with the interplanetary magnetic field *Bz* component. EOF2 captures separately the cusp current signature and *By*-related variability. Compared to existing models, MFACE yields significantly better spatial resolution, reproduces typically observed FAC thickness and intensity, improves on the magnetic local time (*MLT*) distribution, and gives the seasonal dependence of FAC latitudes and the NBZ current signature. MFACE further reveals systematic dependences on *By*, including 1) Region-1/Region-2 topology modifications around noon; 2) imbalance between upward and downward maximum current density; 3) *MLT* location of the Harang discontinuity. Furthermore, our procedure allows quantifying response times of FACs to solar wind driving at the bow shock nose: we obtain 20 minutes and 35–40 minutes lags for the FAC density and latitude, respectively. **Citation:** He, M., J. Vogt, H. Lühr, E. Sorbalo, A. Blagau, G. Le, and G. Lu (2012), A high-resolution model of field-aligned currents through empirical orthogonal functions analysis (MFACE), *Geophys. Res. Lett.*, *39*, L18105, doi:10.1029/2012GL053168.

1. Introduction

[2] Field-aligned currents (FACs) are important agents for energy and momentum transport between the solar wind-magnetosphere system and the polar ionosphere-thermosphere system. Empirical modeling of the FACs system is required by both the ionosphere-magnetosphere coupling community and the geomagnetic modeling community [e.g., *Lukianova and Christiansen*, 2006; *Vennerstrøm et al.*, 2007], but is challenging due to dynamics and complexity of FACs. The basic spatial pattern of FACs was retrieved using TRIAD magnetic measurements [*Iijima and Potemra*, 1976], in which FACs follow a double ring pattern with the poleward Region-1 (R1 for short) portion and the equatorward Region-2 (R2) currents. Through magnetogram inversion techniques using ground-based measurements, the FAC system was found to be controlled by interplanetary magnetic field (IMF) and solar wind (SW) conditions [e.g., *Feldstein and Levitin*, 1986]. FACs were firstly quantitatively modeled through taking the divergence of the ionospheric currents [e.g., *Foster et al.*, 1989; *Kamide et al.*, 1981]. The models were confirmed and improved by space-based magnetic measurements, including datasets of Dynamics Explorer 2 during 1981–1983 [*Weimer*, 2001], Iridium constellation [*Waters et al.*, 2001], and Magsat and Ørsted dataset [*Papitashvili et al.*, 2002]. For a comparison between different models, readers are referred to *Stauning et al.* [2005]. Taking advantage of the enormous database and continuous IMF/SW coverage, the above models parameterized the global-scale FAC geometry and its climatology. However, the models suffer from low spatial resolution, characterized by low current density associated with large thickness [e.g., *Stauning et al.*, 2005]. This resolution problem arises from the inherent limitation of the global fitting procedures through which the input data are averaged in separate sectors according to some 'governing' parameters [*Anderson and Christiansen*, 2003; *Stauning et al.*, 2005]. Furthermore, many aspects of FAC dynamics are not contained in existing models, such as the seasonal variation of FAC latitude dependence [e.g., *Anderson et al.*, 2008]. In the present work we try to overcome the above shortcomings by constructing a Model of FACs through Empirical Orthogonal Function analysis (MFACE).

2. Data Analysis and Methodology

[3] The CHAMP satellite was launched into orbit with inclination of 87.3°, at ~440 km altitude in 2001, decaying to ~310 km at the beginning of 2010. For this study, 1s-averaged CHAMP magnetic vector data from ~53,000 orbits collected during 2001–2010 are used. The geomagnetic latitude (*MLat*) and geomagnetic local time (*MLT*) refer to altitude adjusted corrected geomagnetic (AACGM) coordinate.

[4] First, we calculate magnetic perturbation vectors through subtracting the POMME-6 model [*Maus et al.*, 2006], both the internal and external parts, from the CHAMP data. Then for each auroral oval crossing, we identify a reference point of Auroral Current Centre (ACC), and estimate a meridian profile of current density by the procedures demonstrated in Figure 1 through an example. Figure 1a presents time series of each $\delta \boldsymbol{B}$ component. Each of the three components is employed to wavelet analysis with a mother function of Paul wavelet of order 3. The

[1]School of Engineering and Science, Jacobs University Bremen, Bremen, Germany.
[2]Deutsches GeoForschungsZentrum Potsdam, Potsdam, Germany.
[3]Institute for Space Sciences, Bucharest-Magurele, Romania.
[4]Heliophysics Science Division, NASA Goddard Space Flight Center, Greenbelt, Maryland, USA.
[5]High Altitude Observatory, NCAR, Boulder, Colorado, USA.

Corresponding author: M. He, School of Engineering and Science, Jacobs University Bremen, Campus Ring 1, D-28759 Bremen, Germany. (m.he@jacobs.university.de)

0094-8276/12/2012GL053168

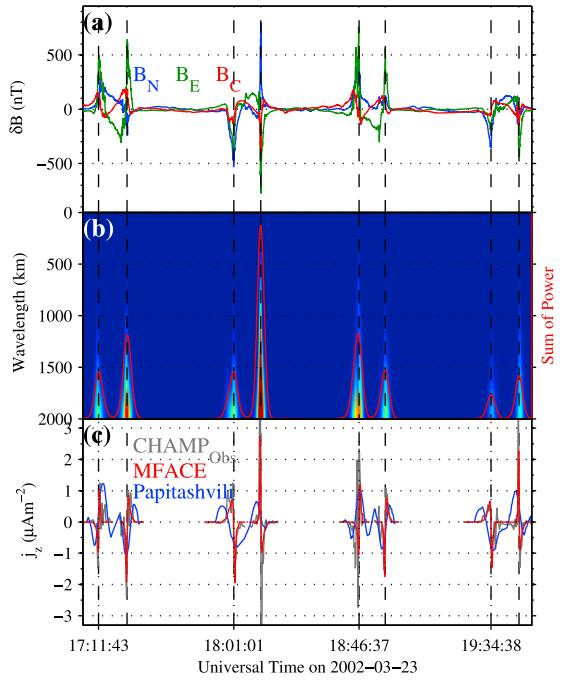

Figure 1. Example for the Auroral Current Centre identification and current density estimation. (a) Time series of $\delta \boldsymbol{B}$ in North-East-Center coordinates. $\delta \boldsymbol{B}$ is the magnetic perturbation vector obtained from CHAMP measurements after the subtraction of POMME. (b) The sum (color code) of three wavelet spectra for series shown in Figure 1a, and its integral (red line) between 200–1600 km. (c) Estimated current density (gray lines), associated with outputs of MFACE (red lines) and the model (blue lines) of *Papitashvili et al.* [2002]. In each panel, dashed lines indicate the Auroral Current Centre.

resulting spectra are summarized in Figure 1b. The obtained spectrum is further integrated in the scale range of 200–1600 km, and shown with the red line in Figure 1b. The maximum in each quarter orbit (0°– max. *MLat*) is referred as the ACC, located at $MLat_{ACC}$ and marked by dashed lines in Figure 1. In a 20°-MLat-width interval centered at $MLat_{ACC}$, the perturbations $\delta \boldsymbol{B}$ are used for minimum variance analysis (MVA). For the MVA, we define an Orbit-Geomagnetic (OGM) coordinate system. In the OGM frame, $\hat{\mathbf{z}}$ is along the local POMME magnetic field, $\hat{\mathbf{x}}$ is in the direction of the cross product of $\hat{\mathbf{z}}$ and the orbit normal in northern direction, and $\hat{\mathbf{y}}$ completes the right-handed orthogonal system. The OGM system is an inertial frame for uniform background geomagnetic field directions, superior to Geomagnetic coordinates defined with geomagnetic East and West [e.g., *Wang et al.*, 2005] which quickly rotate by ~180° around its $\hat{\mathbf{z}}$ axes every time when the satellite goes through maximum *MLat.* MVA in the x-y plane produces the component of $\delta \boldsymbol{B}$ along the direction of minimum (maximum) variance. Assuming sheet-like FACs, the current density j_z is determined as a function of *MLat* according to Ampere's law, and then mapped to 110 km altitude. Small-scale fluctuations are reduced using a Butterworth low-pass filter with a cutoff frequency equivalent to 220 km wavelength or ~55 km spatial resolution. Resulting profiles are interpolated to a *MLat* grid with an origin referring to ACC, termed $\Delta MLat_{grid}$.

[5] In the second step, the gridded profiles are binned in each hemisphere for Empirical Orthogonal Function (EOF) analysis [cf. *Jolliffe*, 2002; *He et al.*, 2011], through which profiles are decomposed into linear combinations of EOFs, $j(\Delta MLat_{grid}) = \bar{j}(\Delta MLat_{grid}) + \sum_i s_i \cdot EOF_i(\Delta MLat_{grid})$. Here, $\bar{j}$ is the average of all profiles, s_i is the score for EOF_i, and EOFs are mutually uncorrelated data-derived functions arranged in descending order by the variance they account for (see also the auxiliary material).[1] The corresponding contribution of EOF_i to the total variance is ranked in Figure 2a.

[6] After each j_z profile is represented with factors of a $MLat_{ACC}$ and a group of s_i, a j_z model could be constructed through parameterizing the factors. The $MLat_{ACC}$ is regressed as a function of *MLT*, Day of Year (*DoY*), IMF clock angle θ_{IMF} in GSM, IMF component in GSM y-z plane B_t, IMF magnitude B, solar wind speed v_{SW} and AE index. For each profile, the parameters refer to the moment when CHAMP passes $MLat_{ACC}$. Mathematically,

$$\begin{aligned} MLat_{ACC}(MLT, DoY, \theta_{IMF}, B_t, B, v_{SW}, AE) \\ = \alpha_0 + \sum_{j=1}^{4} \alpha_{MLT}^{(j)} e^{(j\cdot MLT/24)\cdot 2\pi i} + \sum_{j=1}^{2} \alpha_{DoY}^{(j)} e^{(j\cdot DoY/365.25)\cdot 2\pi i} \\ + \sum_{j=1}^{3} \alpha_{IMF}^{(j)} e^{j\cdot\theta_{IMF}\cdot i} + \alpha_{B_t} B_t + \alpha_\Phi \Phi(\theta_{IMF}, B_t, B, v_{SW}) \\ + \alpha_{AE} AE + \ldots(\text{interaction and squared terms}) \end{aligned} \quad (1)$$

Here, $i = \sqrt{-1}$, Φ is the empirical polar cap potential [*Boyle et al.*, 1997], and α's are coefficients to be determined. We exclude outliers characterized by a residual larger than expectation at the 5% significance level. Since the IMF parameters refer to the Earth bow shock nose, a delay is taken into account through replacing θ_{IMF}, B_t, B, v_{SW} in equation (1) with $\theta_{IMF}(\delta t)$, etc. As indicated by the green lines in Figure 2b, the best $MLat_{ACC}$ model fit is obtained for 35–40 minutes lag. When comparing the model predictions for local summer with winter, the summer current is located at higher latitude around noon by 2–4°, consistent with *Wang et al.* [2005], but at lower latitude around midnight, in line with detections of TRIAD and DMSP [*Fujii et al.*, 1981; *Ohtani et al.*, 2005]. The green dashed lines in Figure 3 for $Bz = -5$nT indicates an example of this variability.

[7] Then, each s_i is fitted with the same function as equation (1). For the fit, we exclude profiles according to the following thresholds: 1) satellite velocity component parallel to the MVA current sheet normal less than 3 km/s, corresponding to an attack angle larger than ~67°; 2) maximum/minimum eigenvalue ratio (a MVA significance measure) less than 2; and 3) angle between the MVA current sheet normal and that suggested by the $MLat_{ACC}$ model larger than 45°, to ensure the estimated sheet orientation is consistent with the statistical R1/R2 rings. Filled portions of the boxes in Figure 2a give the fractions of variance explained by MFACE. The sum of filled fractions, termed R_j^2, quantifies the quality of total density regression. For the first time, the performance of a FAC model is assessed quantitatively. Blue lines in Figure 2b show the R_j^2 as a

[1] Auxiliary materials are available in the HTML. doi:10.1029/2012GL053168.

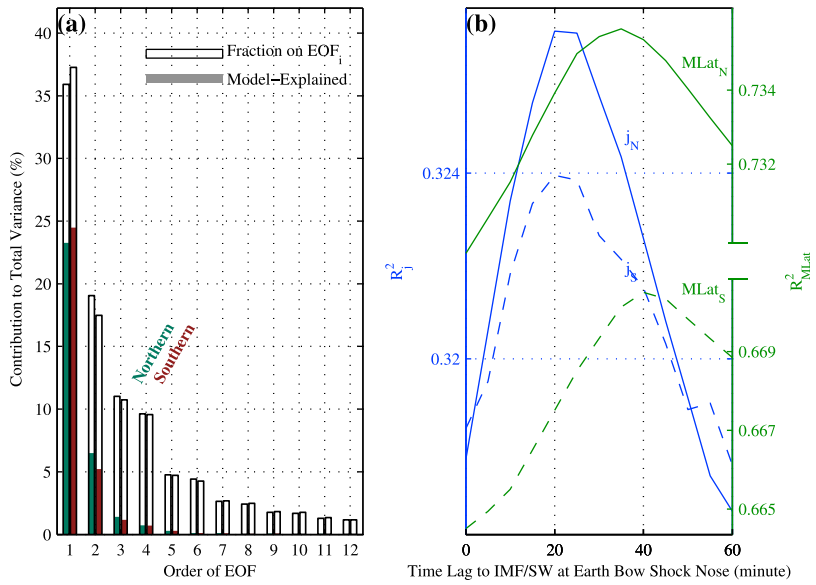

Figure 2. (a) Distribution (the black open boxes) of variance with EOF order, and the corresponding fractions (colorized filled portions) captured by MFACE, for Northern (left) and Southern (right) hemisphere. (b) Efficiencies of the FAC density model (blue) and of the FAC latitude model (green) as functions of time delay to the IMF/SW driving at the bow shock nose, for the Northern (solid) and Southern (dashed) hemisphere.

function of time delay to the IMF/SW. Comparing with the R^2_{MLat} peaks in green, the two R^2_j peaks in blue at 20 minutes suggest that FAC intensity responds quicker than FAC latitude to solar wind driving. Note that besides the Φ, we tested against other coupling functions for IMF/SW control such as the merging electric field, the Akasofu parameter and the Newell function [*Newell et al.*, 2007, and references therein], but found Φ to be the most effective in maximizing R^2_j. Among geomagnetic indices, the AE index is more effective than the Ap, PC, and AL. Since FACs and Φ respond nonlinearly to interplanetary driving [e.g., *Anderson and Korth*, 2007, *Hairston et al.*, 2005], MFACE may potentially be improved through adjusting equation (1).

[8] Finally, MFACE is constructed:

$$j(MLat, MLT, DoY, \theta_{IMF}, B_t, B, v_{SW}, AE) = \bar{j}(\Delta MLat) + \sum_{i=1}^{12} s_i(MLT, DoY, \theta_{IMF}, B_t, B, v_{SW}, AE) \cdot EOF_i(\Delta MLat) \quad (2)$$

Here, $\Delta MLat = MLat - MLat_{ACC}(MLT, DoY, \theta_{IMF}, B_t, B, v_{SW}, AE)$. As an example, Figure 1c presents the modeled current density (red), which is much closer to the CHAMP-derived profiles (gray) in both intensity and extension than the prediction (blue) of *Papitashvili et al.* [2002]. For forecast purposes, we build a model for the AE index using equation (1) after replacing AE with $\overline{B_s^{1h}}$, which is the integral of B_s (equals to B_z when $B_z < 0$, equals to 0 when $B_z > 0$) in the preceding hour [*Arnoldy*, 1971].

3. Results and Discussions

[9] Figure 3 presents the polar distribution of FACs at moderate conditions as a function of IMF clock angle, season and hemisphere, calculated from MFACE. In morphology, all patterns fit the canonical R1/R2 diagram very well [*Iijima and Potemra*, 1976]. In magnitude, the hemispherical integrated FAC intensity (top labels) ranges from ~0.7 to ~3.5 MA in line with existing models [e.g., *Papitashvili et al.*, 2002]. The maximum current (bottom labels) ranges from ~0.5 to ~2.0 μA/m^{-2}, more intense than predictions of existing models and close to individual events [e.g., *Wang et al.*, 2005]. In latitudinal extension, the R1 peak spans 2–3°, as typically observed [e.g., *Iijima and Potemra*, 1978]. For seasonal dependence, intensities are weaker during local winter than summer and equinox, consistent with observations from TRIAD and DMSP [*Fujii et al.*, 1981; *Ohtani et al.*, 2005]. For *MLT* dependence, the downward and upward currents maximize typically in the prenoon and postnoon sector respectively, as marked by crosses, in agreement with TRIAD observations [e.g., *Iijima and Potemra*, 1978]. For IMF dependence, the most remarkable feature is the *Bz*-dominated size and strength of the FAC pattern (also see Figure S1). In particular, under the strongest positive *Bz* (in panels in the top row, marked by the green dots as examples), a current pair named NBZ appears poleward of the R1 sheet, with intensity comparable to *Stauning* [2002]. Besides, the *By* component also influences the FAC configuration remarkably. As indicated by the arrows, in the Northern hemisphere and under positive (negative) *By*, the R1 sheet on the dawn (dusk) side appears to cross noon and extends into R2 sheet on dusk (dawn) side. This *By* dependence has been reported before [e.g., *Anderson et al.*, 2008; *Lu et al.*, 1995; *Stauning et al.*, 2001; *Weimer*, 1999], but it has not been captured so distinctly in existing statistical FAC models. Another *By*-related feature that has not been reported before is the imbalance between upward and downward maximum currents. The dominant peak of the two is highlighted in the plots. In the Northern (Southern) hemisphere and under positive (negative) *By*, the downward current peak dominates the upward peak, but is exceeded by the upward peak when *By* changes orientation.

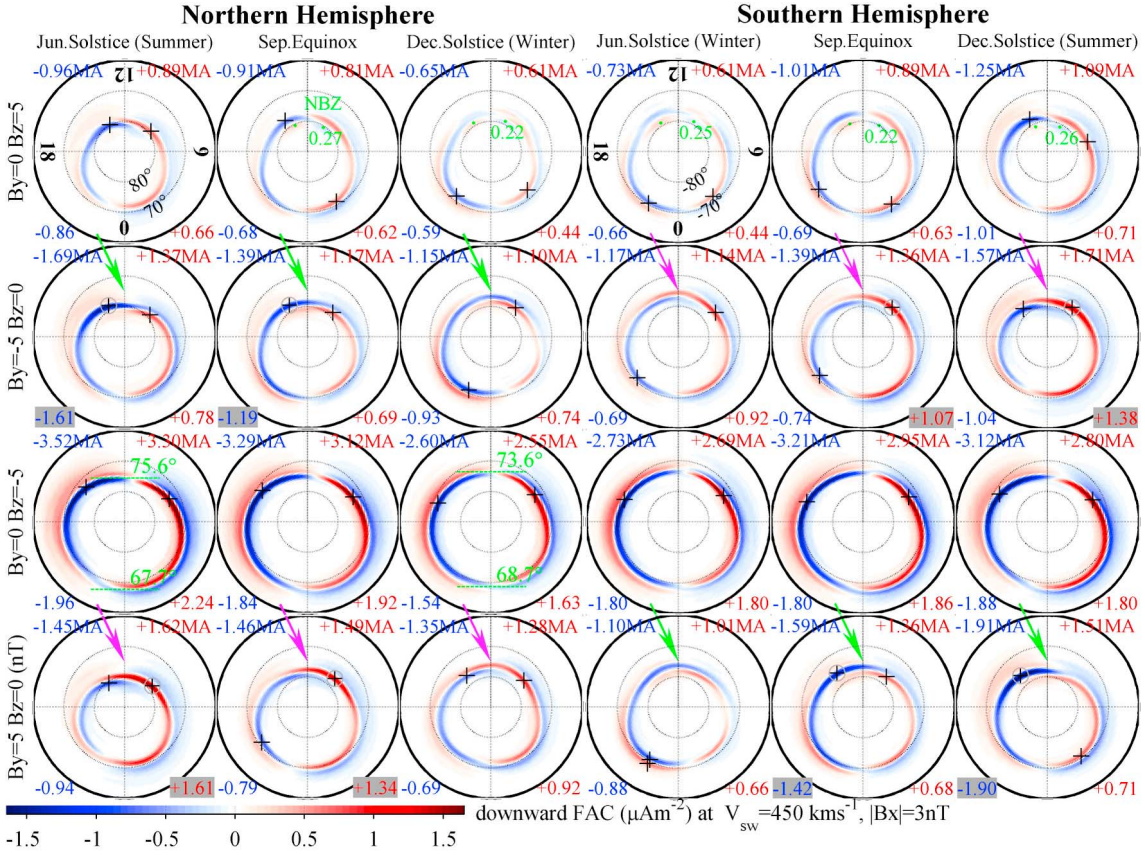

Figure 3. Polar distribution of FAC density in the (left) Northern and (right) Southern hemispheres, organized by IMF clock angle (marked on left margin) and season (marked on top). AE index for each panel is calculated with the AE model mentioned in Section 2. In each panel, numbers in corners show the maximum density (bottom corners, in units of μAm^{-2}) and hemispherical integrated density (top corners, in units of MA), for both the downward (right corners) and the upward current (left corners). Maximum upward and downward current peaks are marked by crosses, and are not balanced: the circled crosses with shadowed values exceed their counterparts by more than 0.3 μAm^{-2} in intensity and 20% in ratio. Arrows in two colors indicate two kinds of noon time FAC topology. The orientation of *By* clearly controls the competition between upward and downward maximum intensities and the noontime topology, which is opposite in the two hemispheres. In panels for $Bz = -5$ nT, green dashed lines present an example for the comparison of FAC latitudes. In panels for $Bz = 5$ nT, paired green dots indicate examples of NBZ signatures [cf. *Stauning*, 2002; *Vennerstrøm et al.*, 2002]. Note that the signature here does not cover all NBZ currents because MFACE does not cover the whole polar cap.

[10] In Figure 4 we separate the contributions from EOF1 and EOF2. Overall, EOF1 plots are controlled by *Bz*, similar to the corresponding panels in Figure 3. In detail, the polarity of the double-ring pattern switches sharply around midnight and noon as indicated by the black arrows. This differs distinctly from the corresponding plots in Figure 3 in which the R1 currents can stretch into the R2 across noon or midnight. Marked by the dotted lines, the midnight switch is identified as a signature of the Harang discontinuity, which appears earlier (later) under positive than under negative *By* in the Northern (Southern) hemisphere, consistent with previous reports [e.g., *Rodger et al.*, 1984]. Different from EOF1, in EOF2 the FAC distribution and its polarity are controlled mainly by *By*. In the Northern (Southern) hemisphere, the positive (negative) *By* is accompanied by a triple-sheet structure comprising a dominant upward current peak flanked by small downward peaks in the morning sector, which shifts to the afternoon sector and changes its polarity as *By* changes orientation. The triple-sheet structure in EOF2 could be read as a signature of cusp (also termed as Region-0) currents. As reviewed by *Cowley* [2000], the *By* component influences near-subsolar reconnection, and determines the tension and flow of newly-opened field lines. For positive (negative) *By* and in the Northern hemisphere, the tension pulls the newly-opened field lines towards dawn (dusk), exciting pairs of East-West oriented current sheets in the morning (afternoon) sector, and simultaneously in the Southern hemisphere pulls field lines toward dusk (dawn) with current sheets occurring in the afternoon (morning) sector. The current system reaches down into the ionosphere and attaches to the R1 ring, thus creating the triple-sheet FAC structure as illustrated in Figures 5 and 6 of *Cowley* [2000]. The dawn-dusk asymmetry of cusp current may contribute significantly to the imbalance between maximum downward and upward current presented in Figure 3. The signature of cusp current is stronger during summer than winter, in accordance with previous reports [*Fujii et al.*, 1981; *Wang et al.*, 2005].

[11] In summary, we developed a FAC model MFACE from CHAMP data with a novel technique based on EOF decomposition. Predictor variables include *MLat*, *MLT*, *DoY*, θ_{IMF}, B_t, B, v_{SW} and AE index. In comparison with existing

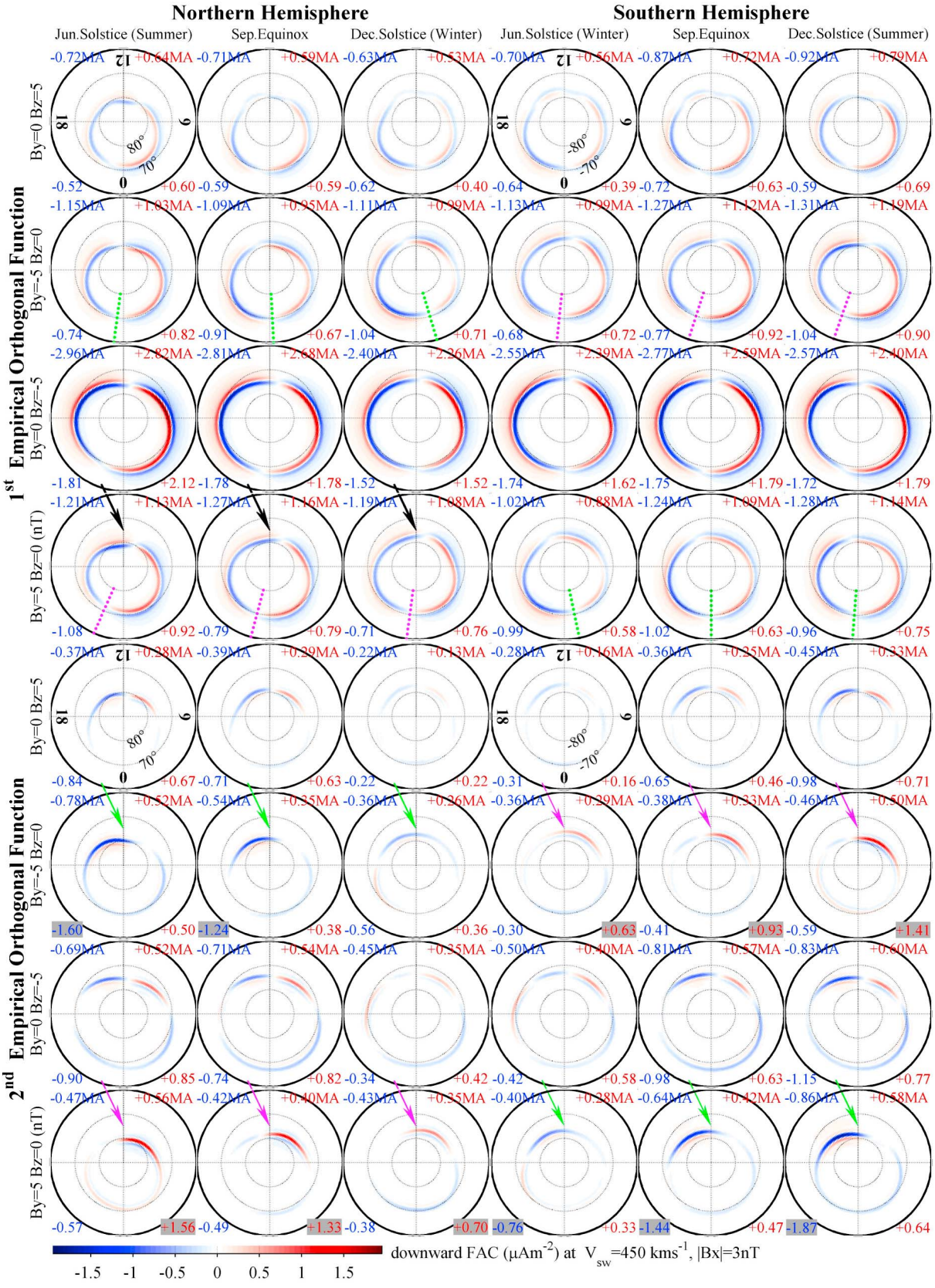

Figure 4. The same plots as in Figure 3 but for separate contributions from (top) EOF1 and (bottom) EOF2. Dotted lines show the *By*-modulated azimuthal location of the Harang discontinuity. Note that the green lines appear later than the corresponding magenta ones in each hemisphere. Black arrows, as examples, indicate that the polarity of the R1/R2 system switches sharply in comparison with the corresponding panels in Figure 3. Colored arrows indicate the *By*-controlled signature of cusp currents, where the two hemispheres show opposite polarities.

models, the most pronounced advantage of MFACE is the enhanced spatial resolution, characterized by more realistic FAC intensity, latitudinal extent and *MLT* distribution. The model also captures the season-*MLT* dependence of FAC location. The daytime FACs appear at higher latitude during local summer than winter, and the seasonal dependence reverses around midnight. Systematic dependences on *By* are manifested in MFACE. Under positive (negative) *By* and in the Northern hemisphere, the dawn (dusk) side R1 current extends across noon into the dusk (dawn) R2 current, and the upward (downward) maximum current exceeds the downward (upward) significantly. *By* modulates also the Harang discontinuity which appears earlier for positive *By* than for negative in the Northern hemisphere. All *By* dependences reverse in the Southern hemisphere. Our EOF decomposition reveals that EOF1 represents mainly the *Bz*-controlled large-scale R1/R2 current pattern whereas EOF2 represents the *By*-controlled cusp current signature. In addition, our procedure allows a rigorous quantitative model assessment and a time delay study of FACs in responding to IMF/SW driving at the subsolar bow shock. The correlation analysis indicates that the response time is about 20 minutes for FAC density and 35–40 minutes for FAC latitude dependence. In brief, MFACE captures most of the known features of FAC climatology, which would contribute to ionosphere-magnetosphere coupling studies and geomagnetic modeling.

[12] **Acknowledgments.** The authors thank Boris Prokhorov, Patricia Ritter and Stefan Maus for their help, and acknowledge the online services provided by GFZ Potsdam (CHAMP data), NGDC (POMME-6.2 coefficients), John Hopkins University APL (AACGM coefficients), and NASA OMNI (IMF/SW and other geophysical parameters). The MFACE code would be released through the link www.faculty.jacobs-university.de/jvogt/mface/ and Source Forge. This work is supported by DFG grant VO 855/3-1.

[13] The Editor thanks Steven Petrinec and an anonymous reviewer for assisting in the evaluation of this paper.

References

Anderson, B. J., and F. Christiansen (2003), What features of field aligned currents might global scale fits miss?, *Eos Trans. AGU*, *84*(46), Fall Meet. Suppl., Abstract SM52D-05.

Anderson, B. J., and H. Korth (2007), Saturation of global field aligned currents observed during storms by the Iridium satellite constellation, *J. Atmos. Sol. Terr. Phys.*, *69*, 166–169, doi:10.1016/j.jastp.2006.06.013.

Anderson, B. J., et al. (2008), Statistical Birkeland current distributions from magnetic field observations by the Iridium constellation, *Ann. Geophys.*, *26*(3), 671–687, doi:10.5194/angeo-26-671-2008.

Arnoldy, R. L. (1971), Signature in the interplanetary medium for substorms, *J. Geophys. Res.*, *76*(22), 5189–5201, doi:10.1029/JA076i022p05189.

Boyle, C. B., P. H. Reiff, and M. R. Hairston (1997), Empirical polar cap potentials, *J. Geophys. Res.*, *102*(A1), 111–125, doi:10.1029/96JA01742.

Cowley, S. W. H. (2000), Magnetosphere-ionosphere interactions: A tutorial review, in *Magnetospheric Current Systems*, *Geophys. Monogr. Ser.*, vol. 118, edited by S. Ohtani et al., pp. 91–106, AGU, Washington, D. C., doi:10.1029/GM118p0091

Feldstein, Y. I., and A. E. Levitin (1986), Solar wind control of electric fields and currents in the ionosphere, *J. Geomagn. Geoelectr.*, *38*(11), 1143–1182, doi:10.5636/jgg.38.1143.

Foster, J. C., T. Fuller-Rowell, and D. S. Evans (1989), Quantitative Patterns of Large-Scale Field-Aligned Currents in the Auroral Ionosphere, *J. Geophys. Res.*, *94*(A3), 2555–2564.

Fujii, R., T. Iijima, T. A. Potemra, and M. Sugiura (1981), Seasonal dependence of large-scale Birkeland currents, *Geophys. Res. Lett.*, *8*(10), 1103–1106, doi:10.1029/GL008i010p01103.

Hairston, M. R., K. A. Drake, and R. Skoug (2005), Saturation of the ionospheric polar cap potential during the October–November 2003 superstorms, *J. Geophys. Res.*, *110*, A09S26, doi:10.1029/2004JA010864.

He, M., L. Liu, W. Wan, and Y. Wei (2011), Strong evidence for couplings between the ionospheric wave-4 structure and atmospheric tides, *Geophys. Res. Lett.*, *38*, L14101, doi:10.1029/2011GL047855.

Iijima, T., and T. A. Potemra (1976), Field-aligned currents in the dayside cusp observed by Triad, *J. Geophys. Res.*, *81*(34), 5971–5979, doi:10.1029/JA081i034p05971.

Iijima, T., and T. A. Potemra (1978), Large-scale characteristics of field-aligned currents associated with substorms, *J. Geophys. Res.*, *83*(A2), 599–615, doi:10.1029/JA083iA02p00599.

Jolliffe, I. T. (2002), *Principal Component Analysis*, 2nd ed., Springer, New York.

Kamide, Y., A. D. Richmond, and S. Matsushita (1981), Estimation of ionospheric electric fields, ionospheric currents, and field-aligned currents from ground magnetic records, *J. Geophys. Res.*, *86*(A2), 801–813, doi:10.1029/JA086iA02p00801.

Lu, G., et al. (1995), Characteristics of ionospheric convection and field-aligned current in the dayside cusp region, *J. Geophys. Res.*, *100*(A7), 11,845–11,861, doi:10.1029/94JA02665.

Lukianova, R., and F. Christiansen (2006), Modeling of the global distribution of ionospheric electric fields based on realistic maps of field-aligned currents, *J. Geophys. Res.*, *111* A03213, doi:10.1029/2005JA011465.

Maus, S., M. Rother, C. Stolle, W. Mai, S. Choi, H. Lühr, D. Cooke, and C. Roth (2006), Third generation of the Potsdam Magnetic Model of the Earth (POMME), *Geochem. Geophys. Geosyst.*, *7*, Q07008, doi:10.1029/2006GC001269.

Newell, P. T., T. Sotirelis, K. Liou, C.-I. Meng, and F. J. Rich (2007), A nearly universal solar wind-magnetosphere coupling function inferred from 10 magnetospheric state variables, *J. Geophys. Res.*, *112* A01206, doi:10.1029/2006JA012015.

Ohtani, S., G. Ueno, T. Higuchi, and H. Kawano (2005), Annual and semi-annual variations of the location and intensity of large-scale field-aligned currents, *J. Geophys. Res.*, *110*, A01216, doi:10.1029/2004JA010634.

Papitashvili, V. O., F. Christiansen, and T. Neubert (2002), A new model of field-aligned currents derived from high-precision satellite magnetic field data, *Geophys. Res. Lett.*, *29*(14), 1683, doi:10.1029/2001GL014207.

Rodger, A. S., et al. (1984), Dawn-dusk (y) component of the interplanetary magnetic field and the local time of the harang discontinuity, *Planet. Space Sci.*, *32*(8), 1021–1027, doi:10.1016/0032-0633(84)90058-8.

Stauning, P. (2002), Field-aligned ionospheric current systems observed from Magsat and Oersted satellites during northward IMF, *Geophys. Res. Lett.*, *29*(15), 8005, doi:10.1029/2001GL013961.

Stauning, P., F. Primdahl, J. Watermann, and O. Rasmussen (2001), IMF By-related cusp currents observed from the Ørsted satellite and from ground, *Geophys. Res. Lett.*, *28*(1), 99–102, doi:10.1029/2000GL012010.

Stauning, P., F. Christiansen, and J. Watermann (2005), On the modeling of field-aligned currents from magnetic observations by polar orbiting satellites, in *Earth Observation With CHAMP*, edited by C. Reigber et al., pp. 371–374, Springer, Berlin, doi:10.1007/3-540-26800-6_59.

Vennerstrøm, S., T. Moretto, N. Olsen, E. Friis-Christensen, A. M. Stampe, and J. F. Watermann (2002), Field-aligned currents in the dayside cusp and polar cap region during northward IMF, *J. Geophys. Res.*, *107*(A8), 1188, doi:10.1029/2001JA009162.

Vennerstrøm, S., F. Christiansen, N. Olsen, and T. Moretto (2007), On the cause of IMF By related mid- and low-latitude magnetic disturbances, *Geophys. Res. Lett.*, *34*, L16101, doi:10.1029/2007GL030175.

Wang, H., H. Lühr, and S. Y. Ma (2005), Solar zenith angle and merging electric field control of field-aligned currents: A statistical study of the Southern Hemisphere, *J. Geophys. Res.*, *110*, A03306, doi:10.1029/2004JA010530.

Waters, C. L., B. J. Anderson, and K. Liou (2001), Estimation of global field aligned currents using the iridium® System magnetometer data, *Geophys. Res. Lett.*, *28*(11), 2165–2168, doi:10.1029/2000GL012725.

Weimer, D. R. (1999), Substorm influence on the ionospheric electric potentials and currents, *J. Geophys. Res.*, *104*(A1), 185–197, doi:10.1029/1998JA900075.

Weimer, D. R. (2001), Maps of ionospheric field-aligned currents as a function of the interplanetary magnetic field derived from Dynamics Explorer 2 data, *J. Geophys. Res.*, *106*(A7), 12,889–12,902, doi:10.1029/2000JA000295.